Coexistence of Dirac fermion and charge density wave in the square-net-based semimetal $LaAuSb_2$

Xueliang Wu,[1,*] Zhixiang Hu,[2,3,*] David Graf,[4] Yu Liu,[2,5] Chaoyue Deng,[6] Huixia Fu,[6] Asish K. Kundu,[2] Tonica Valla,[7] Cedomir Petrovic,[2,3,8,9,†] and Aifeng Wang[1,2,‡]

[1]*Low Temperature Physics Laboratory, College of Physics and Center of Quantum Materials and Devices, Chongqing University, Chongqing 401331, China*
[2]*Condensed Matter Physics and Materials Science Department, Brookhaven National Laboratory, Upton, New York 11973, USA*
[3]*Department of Material Science and Chemical Engineering, Stony Brook University, Stony Brook, New York 11790, USA*
[4]*National High Magnetic Field Laboratory, Florida State University, Tallahassee, Florida 32306-4005, USA*
[5]*Center for Correlated Matter and School of Physics, Zhejiang University, Hangzhou 310058, China*
[6]*College of Physics and Center of Quantum Materials and Devices, Chongqing University, Chongqing 401331, China*
[7]*Donostia International Physics Center, Donostia - San Sebastián, 20018, Spain*
[8]*Shanghai Advanced Research in Physical Sciences, Shanghai 201203, China*
[9]*Department of Nuclear and Plasma Physics, Vinca Institute of Nuclear Sciences, University of Belgrade, Belgrade 11001, Serbia*

(Received 7 June 2023; revised 20 November 2023; accepted 8 December 2023; published 27 December 2023)

We report a comprehensive study of magnetotransport properties, angle-resolved photoemission spectroscopy (ARPES), and density functional theory (DFT) calculations on self-flux grown $LaAuSb_2$ single crystals. Resistivity and Hall measurements reveal a charge density wave (CDW) transition at 77 K. MR and de Haas-van Alphen measurements indicate that the transport properties of $LaAuSb_2$ are dominated by Dirac fermions that arise from Sb square nets. ARPES measurements and DFT calculations reveal an electronic structure with a common feature of the square-net-based topological semimetals, which is in good agreement with the magnetotransport properties. Our results indicate the coexistence of CDW and Dirac fermion in $LaAuSb_2$, both of which are linked to the bands arising from the Sb square net, suggesting that the square net could serve as a structural motif to explore various electronic orders.

DOI: 10.1103/PhysRevB.108.245156

I. INTRODUCTION

Ternary square-net-based compounds $LaTSb_2$ (T = Cu, Ag, Au) have recently attracted renewed interest due to the observation of anisotropic Dirac fermion, charge density wave (CDW), and superconductivity, suggesting that $LaTSb_2$ can serve as a new candidate for scrutinizing the intertwined orders [1–3]. For example, in the typical compound $LaAgSb_2$, two successive CDW transitions were observed at T_{CDW1} = 207 K and T_{CDW2} = 184 K, respectively [1]. ARPES, NMR, and inelastic x-ray scattering (IXS) measurements indicate that CDW in $LaAgSb_2$ is driven by the nesting of Dirac-like bands [3–5]. Dirac-like bands are theoretically predicted to originate from the band folding of the Sb square net and have been experimentally verified by ARPES and magnetotransport measurements [3,6,7]. Superconductivity at T_c = 0.3 K was observed at ambient pressure and can be increased to T_c = 1 K by high pressure [2]. The theoretical calculation demonstrates that the Sb square net is also crucial for the emergence of superconductivity [2]. These investigations indicate that the Sb square net is the key structural motif responsible for the Dirac dispersion, CDW, and superconductivity [1–3].

$LaTSb_2$ crystallizes in a tetragonal $HfCuSi_2$-type structure (P4/nmm, No. 129) featured by alternatively stacking layers of the Sb square net, TSb, and La along the c axis. Interestingly, it has been theoretically and experimentally demonstrated that the electronic structure associated with the Sb square net is tunable by its chemical environment, that is, the structural configuration or magnetism of adjacent layers [8,9]. In fact, the physical properties, including the lattice parameters, the CDW transition temperature (T_{CDW}), and the superconducting transition temperature (T_c) vary systematically in the sequence of Cu, Au, and Ag. For example, $LaCuSb_2$ shows superconductivity below T_c = 0.9 K without CDW transition [10–12], $LaAuSb_2$ shows the CDW transition at 88 K and superconductivity at 0.64 K [13], $LaAgSb_2$ shows two CDW transitions at 207 K and 184 K [1] and superconductivity at 0.3 K [2]. Although the relationship between CDW and superconductivity in $LaAuSb_2$ has been investigated by means of doping, magnetotransport, and pressure measurements [13–16], the electronic structure and topological properties of $LaAuSb_2$ have been largely unexplored. Therefore, it is of great interest to characterize the electronic structure and physical properties of $LaAuSb_2$, which could deepen our understanding of the intertwined orders associated with the Sb square net and their interaction with the neighboring layers.

In this paper, we study the electronic structure and physical properties of $LaAuSb_2$ single crystals via density functional

*These authors contributed equally to this work.
†cedomir.petrovic@stonybrook.edu
‡afwang@cqu.edu.cn

 ©2023 American Physical Society

theory (DFT) calculations, magnetotransport, and ARPES measurements. The in-plane resistivity reveals a CDW transition at $T_{CDW} = 77$ K. A remarkable magnetoresistance (MR) develops below T_{CDW} and reaches the maximum value of 16% at 2 K and 9 T. However, no anomaly corresponding to the CDW transition was found in the specific heat data, suggesting that the Fermi surface gap and structural distortion induced by the CDW transition are weak. Kohler's rule is violated in $LaAuSb_2$, which can be attributed to the multiband effects, especially in the CDW state with the reconstructed Fermi surfaces. Hall measurements indicate that the transport properties are dominated by the hole-type carriers, and the carrier concentration is significantly suppressed by the formation of the CDW order. Quantum oscillation was probed by two methods, i.e., magnetization measurements up to 9 T and torque measurements up to 35 T, which are consistent with each other. From the fast Fourier transform (FFT) spectra for the de Haas-van Alphen (dHvA) oscillation data, $F = 10.9$, 54.7, 1021.4, and 1702.3 T can be obtained. Further analysis of dHvA oscillation data reveals that the Fermi pocket corresponding to $F = 54.7$ T has a quasi-two-dimensional (quasi-2D) character with a small effective mass and nontrivial Berry phase, indicating the existence of Dirac fermion. Further, we directly probe the band structure using ARPES measurements. Both the quantum oscillation and ARPES data can be well interpreted by the electronic structure calculated by the density functional theory, where the Dirac bands can be identified along the Γ-M line and X point in the Brillouin zone. Hence, our study indicates that the Dirac states are indeed present in the CDW compound $LaAuSb_2$.

II. METHODS

A. Experimental details

Single crystals of $LaAuSb_2$ were grown by the self-flux method with excess Au and Sb as flux [17]. Mixtures of La chunks, Au wires, and Sb lumps in the ratio of $La_{0.045}Au_{0.091}Sb_{0.864}$ were loaded into an alumina crucible and then sealed in an evacuated quartz tube. The sealed quartz tubes were slowly heated to 1180 °C, held for 2 h, and then cooled to 670 °C at a rate of 3 °C/h to grow single crystals. Shiny centimeter-sized single crystals can be obtained by decanting the excess flux using a centrifuge.

Powder XRD data were collected using a PANalytical powder diffractometer (Cu K_α radiation). The element analysis was performed using energy-dispersive x-ray spectroscopy (EDX) in a Thermo Fisher Quattro S Environmental scanning electron microscope (SEM). The instrumental error for La, Au, and Sb is 8%, 12%, and 6%, respectively. Specific heat and magnetotransport measurements up to 9 T were conducted on polished crystals to remove Sb flux droplets on the surface in a Quantum Design DynaCool Physical Properties Measurement System (PPMS-9T). Magnetization was measured using the Quantum Design VSM option in PPMS-9T. The magnetic torque was measured using a piezoresistive cantilever in a 35 T resistive magnet at the National High Magnetic Field Laboratory (NHMFL) in Tallahassee. Electrical resistivity ρ_{xx} was measured using a standard four-probe method. Hall resistivity ρ_{yx} was measured using a four-terminal technique by switching the polarity of the magnetic field to eliminate contributions from ρ_{xx}. The ARPES experiments were performed at the Electron Spectro-Microscopy (ESM) 21-ID-1 beam line of the National Synchrotron Light Source II. The beam line is equipped with a Scienta DA30 electron analyzer, with base pressure $\sim 2 \times 10^{-11}$ mbar. The total energy and the angular resolution was ~15 meV and ~0.1°, respectively.

Magnetization, specific heat, and magnetotransport measurements (including in-plane resistivity, Hall resistivity, and magnetoresistance) were performed on a bar-shaped single crystal with a dimension of $2 \times 1 \times 0.2$ mm^3 and a weight of 1.1 mg. The out-of-plane resistivity, magnetic torque, and ARPES measurements were performed on different crystals from the same batch. The out-of-plane resistivity sample is prepared by cutting the crystals into a rod with a dimension of $0.5 \times 0.5 \times 0.8$ mm^3, where the long side of the rod is along the crystallographic c axis. A small crystal with a dimension of $0.6 \times 0.5 \times 0.2$ mm^3 is used for magnetic torque measurements. The dimension of the crystal used for ARPES measurements is about $2 \times 2 \times 0.5$ mm^3. We would like to point out that the physical properties inferred from various measurements are consistent with each other, and no signature of inhomogeneity was found.

B. Theoretical methods

The first-principles calculations were performed using the Vienna *ab initio* simulation package (VASP) [18,19] in the framework of density functional theory (DFT). The generalized gradient approximation (GGA) of Perdew-Burke-Ernzerhof (PBE) [20] was implemented for the exchange-correlation potential. The projected-augmented wave (PAW) pseudopotential [21] was adopted with an energy cutoff of 400 eV as the basis set. A tetragonal cell in $P4/nmm$ space group with the experimental lattice constants was taken. In structural optimizations, all atoms were fully relaxed within the energy convergence threshold of 10^{-6} eV until the residual force on each relaxed atom was less than 0.001 eV/Å. A Γ-centered Monkhorst-Pack k-point mesh of $28 \times 28 \times 12$ was adopted for sampling the first Brillouin zone. To emphasize the effects of spin-orbital coupling (SOC), the electronic properties of $LaAuSb_2$, including band structure, density of states (DOS), and Fermi surface were obtained with SOC taken into account. The analysis and visualization of the Fermi surfaces were implemented via IFERMI software [22].

III. RESULTS AND DISCUSSION

A. XRD, resistivity, and specific heat

Figure 1(a) shows the crystal structure of $LaAuSb_2$, which is composed of alternatively stacking the Sb^{1-} square net, anti-PbO type $[AuSb]^{2-}$ layer along the c axis, separated by La^{3+} ions. As shown in Fig. 1(b), the powder x-ray diffraction (PXRD) pattern of $LaAuSb_2$ can be well refined using a tetragonal structure (space group $P4/nmm$, No. 129) with lattice parameters $a = 4.436(2)$ Å, $c = 10.439(2)$ Å. The atomic ratio determined by EDX is found to be La: Au: Sb = 25.5: 25.3: 49.2 with a standard deviation of 2%, suggesting that our crystals are homogeneous. Further, the core level

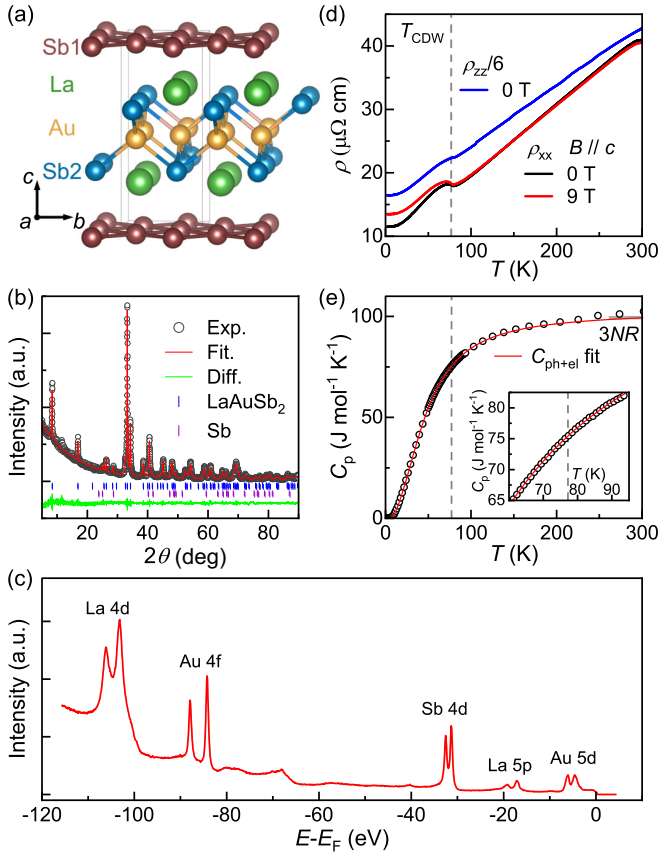

FIG. 1. (a) The crystal structure of $LaAuSb_2$. Sb1 and Sb2 denote the Sb located in the Sb square net and anti-PbO type AuSb layer, respectively (b) Refined powder x-ray diffraction (PXRD) pattern for $LaAuSb_2$. Weak peaks corresponding to a small amount of residual Sb flux were observed in the PXRD pattern. (c) Core-level electronic structure of $LaAuSb_2$, measured using a photon energy of 150 eV. (d) Temperature dependence of in-plane resistivity ρ_{xx} ($j \parallel ab$) at 0 and 9 T and out-of-plane resistivity ρ_{zz} ($j \parallel c$) at 0 T for a $LaAuSb_2$ single crystal, where j is the electric current applied for the resistivity measurements. (e) Temperature dependence of specific heat for $LaAuSb_2$. The inset shows the enlarged view around T_{CDW}. The red line represents the fit using the Debye-Einstein model.

spectra of $LaAuSb_2$ containing all the characteristic peaks of the constituent elements [Fig. 1(c)] also show that the chemical composition at the surface is highly homogeneous. Xiang *et al.* reported that the physical properties of $LaAu_xSb_2$, especially T_{CDW}, depend sensitively on Au stoichiometry [15]. We found that the lattice parameters, chemical composition, and T_{CDW} of our crystal are consistent with $LaAu_{0.94}Sb_2$ reported by Xiang *et al.* [15]. However, the apparent EDX-determined composition in our crystals has a lower Au deficiency, possibly due to the lower resolution of our EDX measurements.

The temperature dependence of the in-plane resistivity $\rho_{xx}(T)$ measured at $B = 0$ and 9 T with electrical current flowing in an in-plane direction ($j \perp c$) is shown in Fig. 1(d). $\rho_{xx}(T)$ decreases linearly with temperature decreasing from room temperature to $T_{CDW} = 77$ K and then shows a slight increase due to the occurrence of CDW transition. T_{CDW} is defined as the minimum of the first derivative of resistivity with respect to the temperature $[d\rho(T)/dT]$, as indicated by the vertical dashed line. The $\rho_{xx}(T)$ below $T_{CDW} = 77$ K is significantly enhanced by a magnetic field of 9 T. In other words, the MR value develops with temperature cooling across T_{CDW}, which reaches the maximum value of MR $= [\rho(B) - \rho(0)]/\rho(0) \times 100\% = 16\%$ at 2 K and 9 T. The out-of-plane resistivity $\rho_{zz}(T)$ with the electrical current running along the c axis ($j \parallel c$) is also shown in Fig. 1(d). The behavior of $\rho_{zz}(T)$ curve is similar to that of $\rho_{xx}(T)$, showing a similar residual resistivity ratio (RRR) of ~ 3 with an anisotropy of $\rho_{zz}(T)/\rho_{xx}(T) \sim 6$. Note that the resistivity increase induced by CDW transition in $\rho_{zz}(T)$ is weaker than that in $\rho_{xx}(T)$, consistent with the in-plane CDW modulation wave as observed in $LaAgSb_2$ [1].

Specific heat measurements were performed to gain further insight into the CDW transition, and the result is displayed in Fig. 1(e). The value of room-temperature specific heat is in good agreement with the Dulong-Petit limit of $3NR$, where $N = 4$ is the atomic number per chemical formula and $R = 8.314\,\mathrm{J\,mol^{-1}\,K^{-1}}$ is the universal gas constant. As shown in Fig. 1(e), the specific heat can be well described by the Debye-Einstein model [23]:

$$C_{\mathrm{el+ph}}(T) = \gamma T + \alpha 9NR\left(\frac{T}{\theta_D}\right)^3 \int_0^{\theta_D/T} \frac{x^4 e^x}{(e^x-1)^2}dx + (1-\alpha)3NR\frac{(\theta_E/T)^2 e^{\theta_E/T}}{(e^{\theta_E/T}-1)^2}, \quad (1)$$

where γ is the Sommerfeld coefficient, and θ_D and θ_E are the Debye and Einstein temperatures, respectively. The coefficients α and $1-\alpha$ denote the contribution of the Debye and Einstein terms to the phonon heat capacity, respectively. The fitting yelds $\alpha = 0.84$, $\gamma = 5.2\,\mathrm{mJ\,mol^{-1}\,K^{-2}}$, $\theta_D = 207$ K, and $\theta_E = 63$ K. θ_D is close to that previously reported in $LaAuSb_2$ ($\theta_D = 196$ K) [13,14], but significantly lower than that in $LaAgSb_2$ ($\theta_D = 260$ K) [2]. From the inset of Fig. 1(d), one can see that no anomaly corresponding to the CDW transition can be detected in the specific heat curve, which is reminiscent of the short-ranged CDW in kagome magnet FeGe [24]. However, unlike in FeGe, in the sister compound $LaAgSb_2$, the structural distortions associated with the two CDW transitions are long ranged, as can be seen in x-ray scattering measurements [1]. $LaAgSb_2$ has a higher T_{CDW} (> 200 K), but also shows a weak anomaly in specific heat and magnetization and the anomaly in resistivity is even weaker than in $LaAuSb_2$ [25]. Assuming that $LaAuSb_2$ shares a similar CDW mechanism with $LaAgSb_2$, the CDW in $LaAuSb_2$ very likely has a long-range nature. The CDW order in $LaAgSb_2$ is suggested to be driven by the Fermi surface nesting [3] resulting in a very large real-space periodicity of ~ 17 nm (CDW1, $\tau_1 \sim 0.026a^*$) but small magnitude of distortions. That, and the absence of CDW gap in ARPES causes only very weak anomalies in physical property measurements [25].

B. MR and Hall measurements

Since the behavior of MR could provide valuable information about the underlying electronic structure, MR as a function of the magnetic field was measured at various temperatures and the results are displayed in Fig. 2(a). The

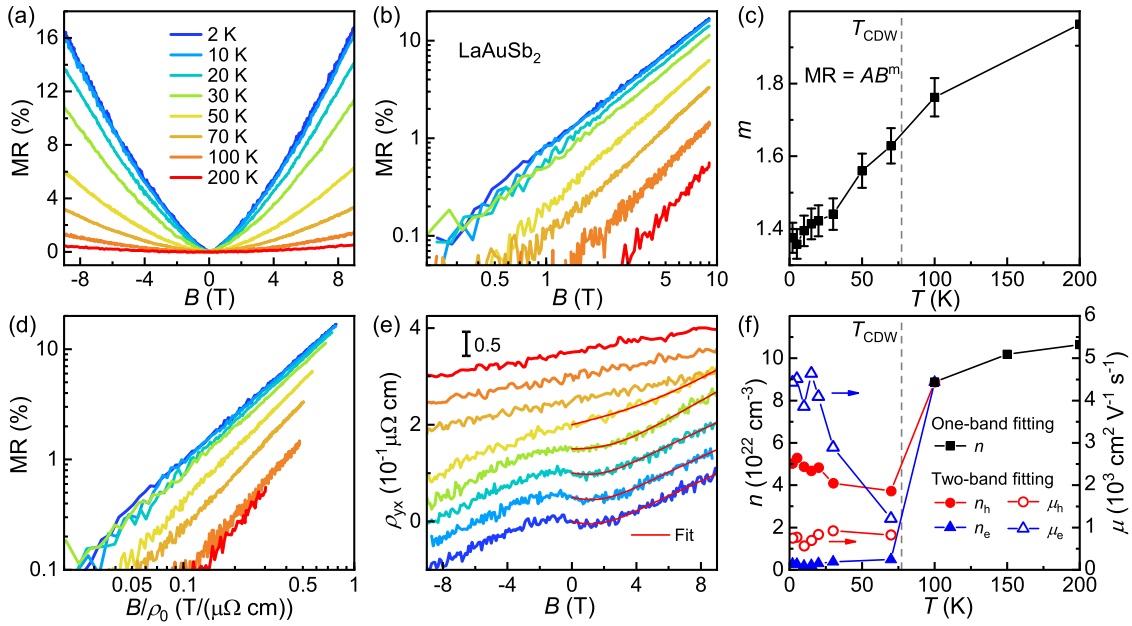

FIG. 2. (a) Magnetic field dependence of MR at various temperatures with $B \parallel c$. (b) Log-log plot of the MR versus B curves. (c) Temperature dependence of the exponent n in $\mathrm{MR} = AB^m$. (d) Kohler plot on log-log scale for $LaAuSb_2$. (e) Hall resistivity ρ_{yx} as a function of the magnetic field at different temperatures with $B \parallel c$. Each subsequent $\rho_{yx}(B)$ curve is shifted upward $0.5 \times 10^{-1} \mu\Omega$ cm for clarity. The fits using the two-band approach are shown by red lines. (f) Temperature dependence of carrier concentration and mobility, which is estimated by the single-band fitting for $T > T_{\mathrm{CDW}}$ and the two-band fitting for $T < T_{\mathrm{CDW}}$. (a), (b), (d), and (e) use the same legend.

maximum MR value is 16% at 2 K and 9 T, which decreases monotonously as the temperature increases and becomes negligibly small when $T > T_{\mathrm{CDW}}$, in good agreement with the $\rho(T)$ data [Fig. 1(d)]. To quantify the evolution of the MR(B) behavior as a function of temperature, we replot the MR(B) data on a log-log scale in Fig. 2(b) and fit MR(B) data to a simple power law $\mathrm{MR} = AB^m$, where A is a constant, m is the exponent proportional to the slope of the log-log scale plot in Fig. 2(b). The resulting m is plotted against temperature in Fig. 2(c). m increases almost linearly from 1.35 at 2 K to 2 at 200 K without significant anomaly at T_{CDW}. $1.35 \leqslant x \leqslant 2$ indicates the possible presence of Dirac linear MR together with parabolic MR of topologically trivial states. In a conventional metal, MR(B) is expected to be parabolic at low fields and it should saturate at high fields, unless perfectly n–p compensated [26,27]. Linear MR was often observed in topological semimetals, which was explained in the context of quantum transport. However, the quantum explanation for linear MR often receives criticism because the classical transport, such as inhomogeneity and open Fermi surface [28,29], could also provide a plausible explanation. Although linear MR is not smoking-gun proof, we point out that it can still be taken as a signature of the Dirac fermion, whereas the more rigorous confirmation would require further evidence from the band structure. Since the presence of Dirac fermion is indeed indicated by DFT calculations, ARPES, and quantum oscillation measurements (see Secs. III C–III F), the linear MR in $LaAuSb_2$ can be attributed to the quantum transport associated with the Dirac fermion.

To further explore the underlying electronic structure associated with MR(B), we analyze the MR by Kohler's rule, which dictates that the MR in a conventional metal obeys a scaling behavior of $\mathrm{MR} = f(B/\rho_0)$ [30], where ρ_0 is the zero-field resistivity at a given temperature. As shown in Fig. 2(d), instead of collapsing onto a single curve as expected by the Kohler rule, MR vs B/ρ_0 curves can be divided into three groups, i.e., the low-temperature part ($T \leqslant 30$ K), the temperatures around T_{CDW} (50 and 70 K), and the high-temperature part ($T \geqslant 100$ K), demonstrating the violation of Kohler's rule. Kohler's rule is expected to be valid in metal with a single type of charge carrier and a single scattering time, which will be violated in materials with multiple scattering times or phase transitions. Thus, the violation of Kohler's rule in $LaAuSb_2$ is expected and can be understood in terms of CDW transition, i.e., carrier types and densities and scattering times will be dramatically altered by the formation of CDW at temperatures around T_{CDW}, while exhibiting a weak temperature dependency at temperatures $T < T_{\mathrm{CDW}}/2$ and $T > T_{\mathrm{CDW}}$ [31], resulting in three different scaling regimes for the MR vs B/ρ_0 curves. Separate Kohler scaling behavior has also been observed in other CDW systems such as $TiSe_2$ and VSe_2 [32,33]. In addition, due to the existence of multiple Fermi pockets, as evidenced by the multifrequencies in quantum oscillations [Fig. 3], nonlinear Hall resistivity [Fig. 2], and measured (in ARPES) and calculated Fermi surface [Figs. 5 and 6], the violation of Kohler's rule in $LaAuSb_2$ could also be interpreted in terms of the multiband scenario.

Hall resistivity $\rho_{yx}(B)$ curves are shown in Fig. 2(e). $\rho_{yx}(B)$ exhibits a nearly linear behavior with a slight slope change around $B = 0$ T for $T \leqslant 70$ K, suggesting a multiband behavior with the dominant hole-type carrier. As the temperature increases, the slope of $\rho_{yx}(B)$ varies slightly in the temperature range of $2 \sim 70$ K. Meanwhile, the slope change around $B = 0$ gradually fades away and becomes invisible when $T \geqslant 70$ K. The slope of $\rho_{yx}(B)$ exhibits a sudden change as the temperature warms across T_{CDW}, which shows a weak

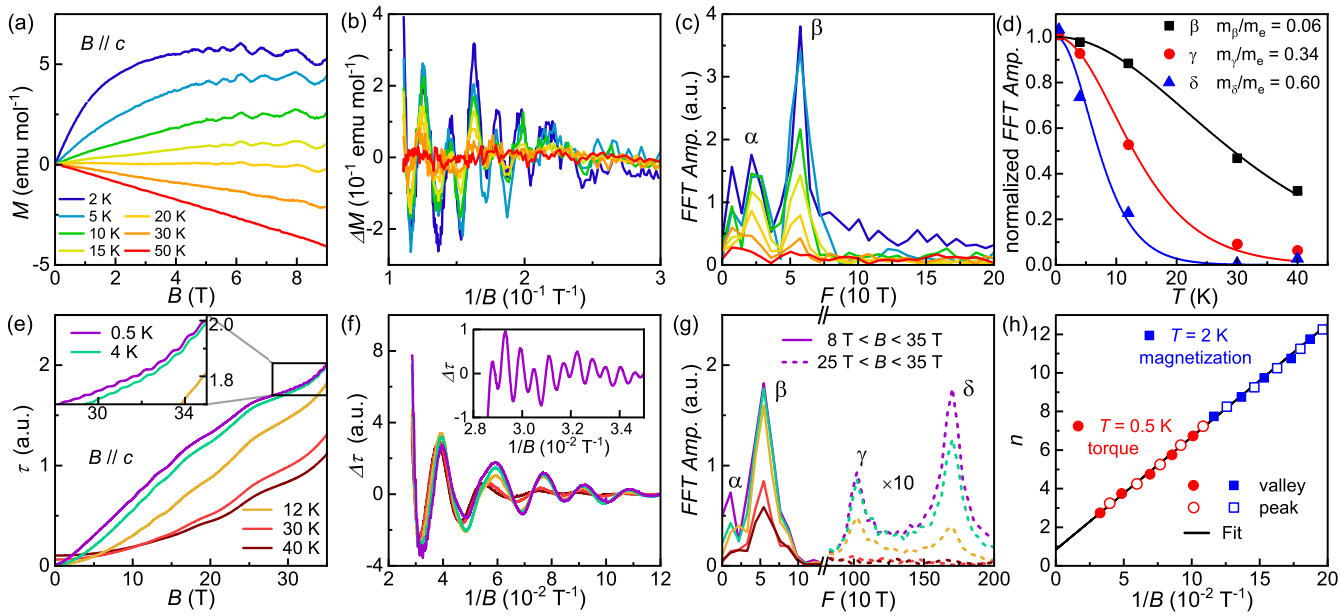

FIG. 3. (a) Isothermal out-of-plane magnetization $[M(B)]$ for $LaAuSb_2$ at various temperatures from 2–50 K. (b) The oscillatory component of magnetization, ΔM. (c) The FFT spectra for the oscillatory component (ΔM) for $B \parallel c$. (d) Temperature dependence of the FFT amplitude of the main frequencies, which is obtained from the FFT spectra for $\Delta\tau$ in (g). Solid lines represent the fits of the LK formula. (e) The field dependence of magnetic torque τ for $LaAuSb_2$ at different temperatures. The inset is the enlarged view of the high-field part of τ as indicated by the black rectangle, where the high-frequency oscillation can be visualized. (f) The oscillatory component of τ for $B \parallel c$. The inset displays a high-frequency oscillatory component obtained by filtering out low-frequency oscillations. (g) FFT spectra for the dHvA oscillation in the magnetic field range of 8 T $< B <$ 35 T. The dashed lines represent the FFT spectra for the dHvA oscillation in the magnetic field range of 25 T $< B <$ 35 T, which are magnified ten times in magnitude for clarity. (h) LL index fan diagram for oscillation component ΔM at 2 K and $\Delta\tau$ at 0.5 K, where the Berry phase extracted from ΔM is in good agreement with $\Delta\tau$. The black line represents a linear fit to all LL indices, which yields an intercept of $n_0 = 0.9$.

temperature dependency with a further increase in temperature. The high-temperature linear $\rho_{yx}(B)$ curves were fitted using a standard single-band model: $d\rho_{yx}(B)/dB = R_H = 1/ne$, where n is the carrier concentration and e is the elementary charge. The low-temperature nonlinear $\rho_{yx}(B)$ curves were analyzed within a two-band approach [34]:

$$\rho_{xy} = \frac{B}{e}\frac{(n_h\mu_h^2 - n_e\mu_e^2) + (n_h - n_e)(\mu_h\mu_e)^2B^2}{(n_h\mu_h + n_e\mu_e)^2 + (n_h - n_e)^2(\mu_h\mu_e)^2B^2}, \quad (2)$$

where $n_h(n_e)$ and $\mu_h(\mu_e)$ correspond to the absolute value of the hole (electron) concentration and the hole (electron) mobility, respectively. The fitting results are plotted in Fig. 2(f). The carriers at 200 K are hole-type with the concentration $n \sim 1.1 \times 10^{23}\,\mathrm{cm}^{-3}$, which is significantly suppressed by the formation of CDW order. The transport properties below T_{CDW} are dominated by the high concentrations of hole-type carriers with a low mobility and the low concentrations of electron-type carriers with a significantly higher mobility. This result is consistent with the calculated band structure, where the Fermi surface is composed of large hole pockets with parabolic bands [Figs. 6(g) and 6(h)] and relatively small electron pockets with linearly dispersing bands [Figs. 6(i) and 6(j)].

C. Temperature dependence of the dHvA oscillations

Quantum oscillation measurements could provide direct information on the electronic structure, and serve as one of the most powerful tools during the study of topological semimetals. dHvA oscillation signals in this paper were probed by two strategies, i.e., the magnetization measurements up to 9 T [Fig. 3(a)] and magnetic torque measurements up to 35 T [Fig. 3(e)]. In Fig. 3(a), we present the isothermal out-of-plane ($B \parallel c$) magnetization at various temperatures for a $LaAuSb_2$ single crystal, where clear dHvA oscillations superimposed on a paramagnetic/diamagnetic background can be recognized at $B > 4$ T. The oscillatory components ΔM extracted by subtracting a smooth background is plotted against $1/B$ in Fig. 3(b). Note that beat patterns can be discerned on the ΔM vs $1/B$ curves, indicating that oscillatory components contain multiple frequencies. From the fast Fourier transform (FFT) analyses of the oscillatory components ΔM, two frequencies of $F_\alpha = 21.5$ T and $F_\beta = 57.4$ T can be derived [Fig. 3(c)].

To probe the possible high-frequency oscillation, magnetic torque measurements up to 35 T were performed on a $LaAuSb_2$ single crystal. The obtained magnetic torque τ and corresponding oscillatory components $\Delta\tau$ data are plotted in Figs. 3(e) and 3(f), respectively, showing a low-frequency oscillation as that in ΔM at first glance and no signature of Zeeman splitting can be identified. Upon a close inspection of the high-field part of magnetic torque curves as shown in the inset of Fig. 3(e), high-frequency oscillation with a weak oscillation amplitude can be discerned. FFT spectra obtained by the FFT analysis in the field range of 8 T $< B <$ 35 T are shown in Fig. 3(g). The main frequency $F_\beta = 54.7$ T is in good agreement with the magnetization measurements. However,

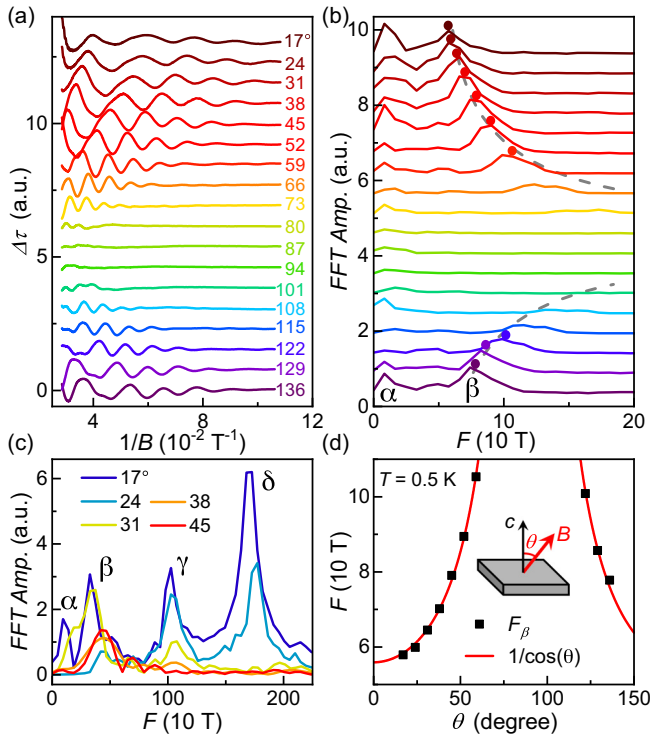

FIG. 4. (a) dHvA oscillations ($\Delta\tau$) at $T = 0.5$ K for different magnetic field orientations. The FFT spectra of the $\Delta\tau$ in the magnetic field range of 8 T $< B <$ 35 T and 25 T $< B <$ 35 T are displayed in (b) and (c), respectively. Data at different field orientations have been shifted for clarity. The dash lines are guides for the eye. (d) The angular dependence of F_α, the solid lines are the fits to $F = F_{2D}/\cos\theta$. (a)–(c) use the same legend.

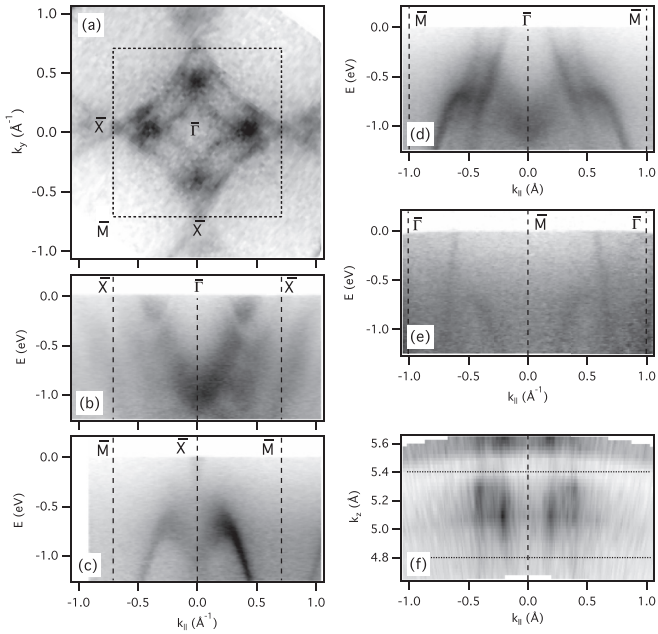

FIG. 5. Electronic structure of $LaAuSb_2$ from ARPES. (a) The Fermi surface. (b)–(e) ARPES spectra along the high-symmetry lines of the surface Brillouin zone, as indicated. Spectra in (a)–(e) were taken using a photon energy of 95 eV, near the π/c plane of the 3D BZ at $T = 15$ K. (f) The Fermi surface in the out-of-plane direction, k_z, at $k_y = 0$, recorded at photon energies in the range from 76–120 eV.

the high-frequency peaks are difficult to recognize in the FFT spectra for 8 T $< B <$ 35 T due to the large difference in the oscillation amplitudes. To get a better visualization of high-frequency FFT spectra, FFT analysis was also performed on the oscillatory components $\Delta\tau$ in the field range of 25 T $< B <$ 35 T where the low-frequency oscillation can be subtracted as the background [inset in Fig. 3(f)], the obtained FFT spectra are magnified tenfold in amplitude and displayed as dash lines in Fig. 3(g). Figure 3(g) shows four frequencies: $F_\alpha = 10.9$ T, $F_\beta = 54.7$ T, $F_\gamma = 1021.4$ T, and $F_\delta = 1702.3$ T. The oscillation frequency is directly related to the cross-sectional area of the Fermi surface normal to the magnetic field A_F through the Onsager relation [35], $F = (\frac{\Phi_0}{2\pi^2})A_F$, where Φ_0 is the flux quantum. Then, A_F for the Fermi pockets associated with F_α, F_β, F_γ, and F_δ are estimated to be $A_{F,\alpha} = 0.10\,\mathrm{nm}^{-2}$, $A_{F,\beta} = 0.51\,\mathrm{nm}^{-2}$, $A_{F,\gamma} = 9.49\,\mathrm{nm}^{-2}$, and $A_{F,\delta} = 15.82\,\mathrm{nm}^{-2}$. These A_Fs correspond to 0.05%, 0.25%, 4.7%, and 7.9% of the total area of the Brillouin zone in the *ab* plane, suggesting that dHvA oscillations arise from small Fermi pockets.

According to the Lifshitz-Kosevich formula [35], the effective mass $m = m^* m_e$ can be obtained by fitting the temperature dependence of the oscillation amplitude to the thermal damping factor R_T, which is defined as:

$$R_T = \frac{\alpha T m^*/\overline{B}}{\sinh\left(\alpha T m^*/\overline{B}\right)}, \tag{3}$$

where $\alpha = 2\pi^2 k_B m_e/e\hbar = 14.69\,\mathrm{T/K}$, $1/\overline{B}$ is the average inverse field when performing FFT analysis. As shown in Fig. 3(c), the fittings yield $m_\beta = 0.06 m_e$ for Fermi surface β, which is comparable to that in (Ca, Sr, Ba, Yb)$MnSb_2$ [36–39] but significantly smaller than $0.16 \sim 0.42 m_e$ in $LaAgSb_2$ [17]. Fermi pockets associated with F_γ and F_δ have larger effective masses. It is well known that effective mass is related to the electronic band curvature $m^* = \hbar^2/[\partial^2 E(k)/\partial k^2]$, and hence, small effective masses in $LaAuSb_2$ could serve as evidence for the presence of Dirac linear dispersion.

In addition to the small Fermi pocket and light effective mass, the Berry phase is another piece of evidence for the Dirac dispersion that could be given by quantum oscillation measurements. A nontrivial π Berry phase is expected for the relativistic Dirac fermions with linear dispersion. According to the Lifshitz-Onsager quantization rule, Landau level (LL) index n is related to $1/B$ by $A_F(\hbar/eB) = 2\pi(n + \gamma - \delta)$, from which the Landau level index fan diagram can be constructed. $\gamma - \delta$ is the phase factor for oscillation, where $\gamma = \frac{1}{2} - \frac{\phi_B}{2\pi}$ and ϕ_B is the Berry phase, δ is a phase offset related to the dimensionality of the Fermi surface and takes values of 0 and $\pm 1/8$, respectively, for 2D and 3D cases. Berry phase ϕ_B is zero for conventional metals while $\pm\pi$ for Dirac fermions. During the analysis of the Berry phase, the minimum of the DOS(E_F) should be assigned with integer LL indices n, that is, the minimum of the Gibbs thermodynamic potential Ω corresponds to the minimum of DOS (E_F). The magnetization M is equal to the derivative of the Gibbs thermodynamic potential at constant temperature and chemical potential, i.e., $M = \frac{\partial\Omega}{\partial B}$. Therefore, there should be a $\frac{\pi}{4}$ phase difference between M

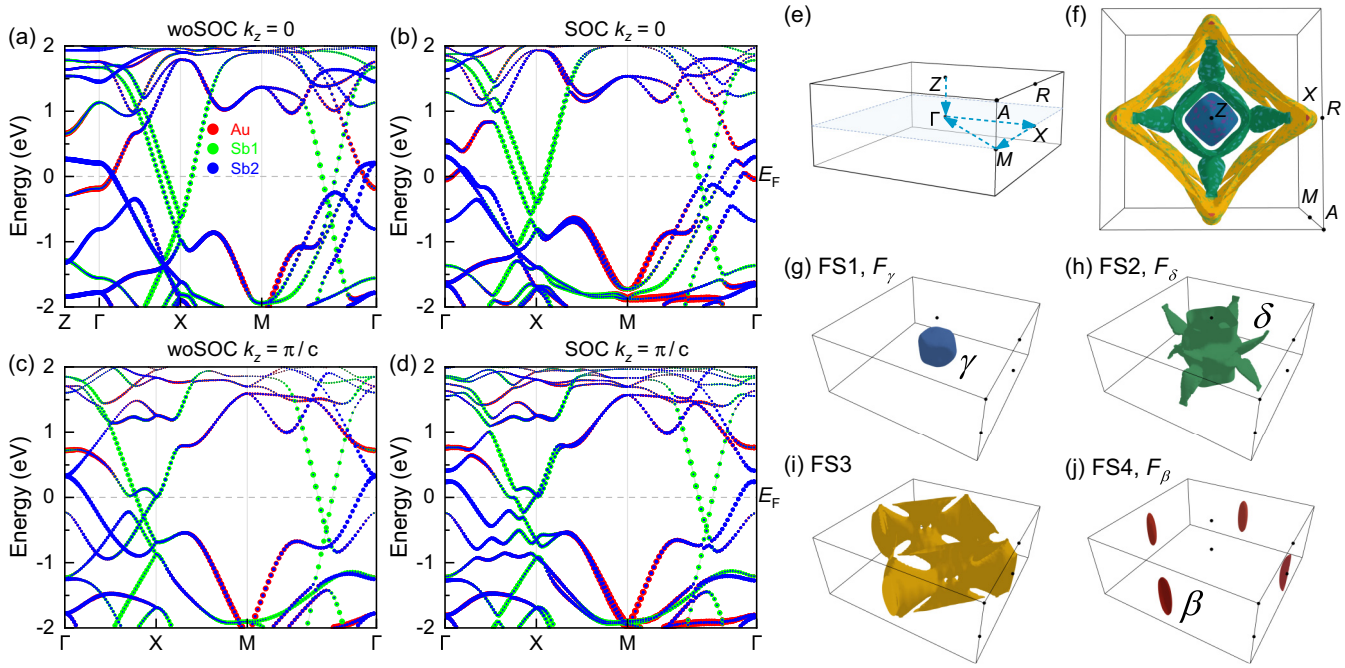

FIG. 6. Calculated band structures of $LaAuSb_2$ without (a) and with (b) spin-orbit coupling at $k_z = 0$. Calculated band structures of $LaAuSb_2$ without (c) and with (d) spin-orbit coupling at $k_z = \pi/c$. Red, green, and blue circles represent the contribution from Au, Sb1, and Sb2 orbitals. The area of the circles represents the relative weight of the orbitals. (e) Three-dimensional (3D) Brillouin zone of $LaAuSb_2$. (f) 3D Fermi surface of $LaAuSb_2$ at $E = -0.01$ eV, which consists of four Fermi pockets plotted separately in (g)–(j) for clarity.

and DOS(E_F) [40]. When the oscillations in magnetization are used to establish a LL fan diagram, the minima of M should be assigned with $n - 1/4$ (where n is an integer). The obtained Landau level index fan phase diagram is plotted in Fig. 3(h), where a nontrivial Berry phase with $\gamma = 0.9$ ($\phi_B = 0.8\pi$) can be deduced from the intercept of the linear fit. This provides evidence for the existence of Dirac fermions in $LaAuSb_2$. Note that the Berry phase deviates from the exact π value. This deviation might stem from the presence of parabolic bands around the Fermi level or from the phase offset related to the dimensionality of the Fermi surface. In addition, although the oscillation in $LaAuSb_2$ is composed of four frequencies, the single-band scenario with F_β can be a good approximation for constructing the LL index fan diagram due to the large difference in the oscillation amplitudes [Figs. 3(a) and 3(e)]. The applicability of this approximation is further verified by the fact that all the points in Fig. 3(h) fall on a straight line with a small deviation (see more details in Supplemental Material, Fig. S2 [41]).

D. Angular dependence of quantum oscillations

To probe the Fermiology and understand the origin of the observed oscillation frequencies, we performed a series of magnetic torque measurements at various magnetic field orientations θ. θ is the angle between the applied magnetic field and the c axis as illustrated by the measurement setup in the inset of Fig. 4(d). The oscillatory components $\Delta\tau$ measured at various tilt angles θ are presented in Fig. 4(a). A high-frequency oscillation with a weak amplitude can be recognized for $\theta \leqslant 31^\circ$ (close to $B \parallel c$). The FFT spectra obtained from the FFT analysis on the field ranges of 8 T $< B <$ 35 T and 25 T $< B <$ 35 T are shown in Figs. 4(b) and 4(c), respectively. F_α and F_β can be discerned in FFT spectra as shown in Fig. 4(b). As θ increases from 17°–136°, F_β progressively shifts to higher frequencies and decreases in amplitude. The oscillation persists to 80°, becomes invisible in the angle range of $80^\circ < x < 101^\circ$, and reappears when $\theta \geqslant 101^\circ$. The divergence in field orientation around $B \parallel c$ ($80^\circ < x < 101^\circ$) is a characteristic of the quasi-2D Fermi surface. For a 2D Fermi surface, the magnetic field projected to the normal axis determines the Landau level quantizations. Thus, the oscillation frequency versus tilt angle curve should follow the inverse of a sinusoidal function. As shown in Fig. 4(d), the F_β vs θ curve can be well described by $F = F_{2D}/\cos(\theta)$, where F_{2D} is the frequency at $\theta = 0$. This indicates that F_β originates from a quasi-2D cylindrical Fermi surface. From the FFT spectra obtained by the FFT analysis on field range 8 T $< B <$ 35 T, one can see that F_γ and F_δ also show a quasi-2D character because with the rotation of magnetic field from the c axis, both F_γ and F_δ decrease in amplitude and become invisible when $\theta > 31^\circ$. Since F_γ persists to a higher angle, Fermi pocket associated with F_γ is more 3D than F_δ.

E. ARPES

ARPES measurements were performed to directly probe the electronic structure of $LaAuSb_2$, as shown in Fig. 5. Figure 5(a) represents the Fermi surface, while Figs. 5(b)– 5(e) show the ARPES spectra along the high-symmetry directions of the surface Brillouin zone (SBZ). Figure 5(f) shows the out-of-plane Fermi surface, measured along the $k_x = k_y$ plane. The spectra from the $\bar{\Gamma}$-$\bar{M}$ line [Fig. 5(d)] show at least two linearly dispersing bands crossing the Fermi level and

forming two diamond-shaped Fermi surfaces (FSs) centered at $\bar{\Gamma}$ [Fig. 5(a)]. The inner states form a diamondlike hole pocket. At first sight, it would seem that the outer bands enclose a large diamond-shaped hole FS. However, this simple picture is deceiving, as demonstrated in Fig. 5(e), which shows the same momentum line but sampled in the second surface BZ. Surprisingly, the outer states now display the electronlike dispersion. The explanation for this is in the fact that the large diamonds are actually formed by extremely anisotropic Dirac cones [5]. However, due to the chemical potential shift relative to the $LaAgSb_2$ case, the Dirac point is much closer to the Fermi level and the contour at that energy looks essentially like a Dirac nodal line. One side of the Dirac-like dispersion along the $\bar{\Gamma}$-$\bar{M}$ is clearly visible in the first BZ, while the other is suppressed in the first, but clearly visible in the second, indicating a strong dependence on ARPES matrix elements, similar to the report by Shi *et al.,* on $LaAgSb_2$ [3]. The large diamondlike contours touch at the zone boundaries ($\bar{X}$ points), forming small electron pockets [Figs. 5(a)–5(c)]. Additionally, we observe high-intensity patches in between $\bar{\Gamma}$ and $\bar{X}$ points [Fig. 5(b)], similar to what has been observed in $LaAgSb_2$ [42].

Overall, the Fermi surface is similar to that measured in $LaAgSb_2$ [3,42] and in good agreement with the DFT calculations shown in Fig. 6 [43]. The estimated area of the inner diamondlike hole pocket is ∼9% of the area of the SBZ. This pocket could then accommodate either γ or δ orbits observed in dHvA, or both, considering its measurable warping in the k_z direction [Fig. 5(f)]. The small electron pockets at $\bar{X}$ points amount to 0.5%. As discussed in the next section, these pockets could be responsible for the oscillation frequency F_β, which is the main transport evidence for the existence of Dirac states in $LaAuSb_2$. The situation with the big diamondlike contour is less obvious. The area of the whole diamond is ∼38% of the area of the SBZ. To observe these orbits in dHvA measurements, much larger fields would be required. If, on the other hand, the observed contour comes from an extremely narrow, anisotropic, and almost neutral ($E_D \approx 0$) Dirac cone that could, in principle, be an origin of the small α orbit. We note that, in the present case, the ARPES experimental resolution was insufficient to observe such small pockets. The estimated Fermi velocities of the inner and outer linear bands along $\bar{\Gamma}$-$\bar{M}$ that form the diamond-shaped FSs are very high: 4.5 and 8.5 eVÅ, respectively, nearly two times higher than that observed in $LaAgSb_2$, consistent with the smaller effective mass estimated from the dHvA oscillations [3].

We note that the sides of the smaller and the larger diamondlike Fermi contours are parallel to each other, providing good nesting conditions. If this is the relevant mechanism, the CDW period would have to be around 20 Å, if the modulation is in the crystallographic a direction, or ∼30 Å, in the more favorable diagonal direction. If, on the other hand, the relevant nesting is within the slightly split sides of the larger diamond, as suggested by Shi *et al.* [3], the period of charge modulation should be much longer than in $LaAgSb_2$, possibly several hundreds of Å, due to the different filling of these elongated Dirac cones. The period of CDW modulations in $LaAuSb_2$ remains to be checked, as detailed structural studies are still lacking. In both nesting scenarios, the nested FS segments are expected to be gapped in the CDW state. However, our ARPES spectra do not display any detectable gaps, similar to some other quasi-2D materials displaying CDW phase [44,45].

F. Electronic structure calculations

In order to better understand the magnetotransport and ARPES data, we performed comprehensive calculations of the electronic structure on $LaAuSb_2$. To emphasize the effects of SOC and k_z dependency, the calculated band structures are plotted into four panels as shown in Figs. 6(a)–6(d), which are consistent with previous reports [43], and share common features with square-net-based topological semimetals, such as $LaCuSb_2$ [11,12], $LaAgSb_2$ [42], $CaMnBi_2$ [46], $YbMnBi_2$ [47], $BaZnBi_2$ [48,49], and ZrSiS [50].

From Figs. 6(a)–6(d), one can see that four bands crossing the Fermi level (E_F), forming a Fermi surface with four Fermi pockets [Fig. 6(f)]. The Fermi pockets are labeled as FS1–FS4 and plotted separately into Figs. 6(g)–6(j) for clarity.

As shown in Figs. 6(a)–6(d), the bands arising from the orbitals of AuSb layer crossing E_F around the Γ point, forming the Fermi pockets of FS1 and FS2. As can be seen in Figs. 6(g) and 6(h), FS1 is a 3D Fermi pocket with a nearly square-shaped cross section while FS2 is a pillarlike 2D Fermi pocket with eight branches along the Γ-X direction (four upward and four downward).

The linear bands crossing E_F at the midpoint of the Γ-M line originate from the $5p_x/5p_y$ orbitals of Sb1 located in the square net, intersect at a Dirac point at ∼0.35 eV below E_F. Note that there is a small gap (55 meV) at the Dirac point, which increases slightly to 71 meV when SOC is taken into account. These linear bands form a large diamond-shaped electron Fermi pocket FS3 as shown in Fig. 6(i). The linear bands and the diamondlike Fermi pocket are the intrinsic features for the square-net structure, which has been experimentally observed in $LaAgSb_2$ [42], $CaMnBi_2$ [46], $YbMnBi_2$ [47], $BaZnBi_2$ [48], and ZrSiS [50].

The linear bands crossing E_F at the X point also arise from the Sb square net, intersecting at two Driac points: one at $E = -0.6$ eV with a small gap of 70 meV and another at $E = -0.4$ eV with a large gap of 350 meV. These gaps at Dirac points are also slightly increased by SOC effects. Notice that these linear bands strongly depend on k_z, indicating a three-dimensional (3D) character. According to their k_z dependency, the inner linear bands should account for the ellipsoidal-shape electron Fermi pocket FS4 centered at the X point [Fig. 6(j)], while the outer linear bands can be assigned to the large diamondlike Fermi pocket FS [Fig. 6(i)].

We first compare the calculated electronic structures with the ARPES data. As shown in Fig. S4 in Supplemental Material [41], the Fermi surfaces exhibit a strong Fermi energy dependency: as the Fermi energy decreases, the pillar-shaped FS2 with eight branches becomes fatter while the diamond-shaped FS3 shrinks and eventually splits into small sheets. From Figs. S4 and S5 in the Supplemental Material [41], we found that the Fermi surfaces at $E = -0.01$ eV match well with the Fermi surface measured by ARPES [Fig. 5(a)]. This Fermi surface could also provide a good explanation for the dHvA oscillation measurements. Through the comparison with the cross-sectional areas of the calculated Fermi pockets with that inferred from the oscillation frequencies (Figs. S4

and S5 in the Supplemental Material [41]), one can see that F_β, F_γ, and F_δ can be assigned to the ellipsoidal-shape FS4 centered at the X point, the inner 3D square-shaped FS1 around Γ point, and the outer pillar-shaped FS2 around Γ point, respectively. These assignments are further verified by the good agreement of band dispersions inferred from the effective masses, ARPES, and DFT calculations.

G. Discussion

Although our magnetotransport, ARPES, and DFT studies provide strong evidence for $LaAuSb_2$ to be a Dirac semimetal, its transport properties deviate from prototypical Dirac semimetals, such as Cd_3As_2, which exhibits a low carrier concentration, ultrahigh mobility, and giant linear MR [51]. The differences originate from different electronic structures: Fermi surface of Cd_3As_2 is composed of a pair of pointlike Fermi pockets with a sharp linear dispersion (the Fermi velocity is determined as $V_x \sim 8$ eVÅ) [52,53]; $LaAuSb_2$ has a more complex Fermi surface with four Fermi pockets, not all of them originating from the Dirac bands. As shown in the ARPES section, Fermi velocities in certain parts of Fermi pockets of $LaAuSb_2$ also have values comparable to that in Cd_3As_2, but the average Fermi velocity is smaller due to the anisotropy and the presence of Fermi pockets with small Fermi velocities. Thus, in $LaAuSb_2$, only a portion of the carriers originate from Dirac bands, and even those are highly anisotropic (elongated), in contrast to highly isotropic 3D-Dirac bands that exist in Cd_3As_2, without conventional bands spoiling the Dirac-like character of carriers.

Recently, the Kagome lattice has attracted great attention due to the observation of CDW, superconductivity, and Dirac fermion. Prime examples include CDW, electronic nematicity, and superconductivity in CsV_3Sb_5 [54,55], CDW in ScV_6Sn_6 [56], and CDW in FeGe antiferromagnet [24]. The emergence of these interesting electronic orders in the kagome lattice comes from the unique lattice geometry of the kagome lattice, which will naturally lead to the flat band, the topological Dirac crossing at the K point, and a pair of van Hove singularities (vHSs) at M points. For example, it is suggested that CDW in CsV_3Sb_5 is triggered by vHSs [57]. From the present study, we see that $LaAuSb_2$ could also simultaneously host Dirac fermions, CDW, and superconductivity, making the square net an ideal model system for investigating these electronic orders.

IV. CONCLUSION

In conclusion, we have studied the physical properties and underlying electronic structure of $LaAuSb_2$ single crystals using magnetotransport and ARPES measurements and DFT calculations. Resistivity and Hall measurements reveal the occurrence of the CDW transition at 77 K. The quantum oscillations and ARPES data reveal quasi-2D Fermi surfaces with nearly massless Dirac fermions, in good agreement with the DFT calculations. Our results indicate that $LaAuSb_2$ hosts CDW and Dirac fermions at the same time, suggesting that the Sb square net could be a building block for designing topological materials with various electronic orders.

ACKNOWLEDGMENTS

The work in Chongqing was financially supported in part by the National Natural Science Foundation of China (Grants No. 12004056 and No. 12104072), the Chongqing Basic Research and Frontier Technology, China (Grants No. cstc2021jcyj-msxmX0661 and No. cstc2021jcyj-msxmX0640), Fundamental Research Funds for the Central Universities, China (Grants No. 2022CDJXY-002 and No. 2023CDJXY-048). Work at BNL was supported by U.S. DOE, Office of Science, and Office of Basic Energy Sciences under Contract No. DE-SC0012704. Work at the National High Magnetic Field Laboratory is supported by National Science Foundation Cooperative Agreement No. DMR-1644779 and the State of Florida. T.V. acknowledges the support from the Red guipuzcoana de Ciencia, Tecnología e Innovación – Gipuzkoa NEXT 2023 from the Gipuzkoa Provincial Council. The authors thank Yan Liu and Guiwen Wang at the Analytical and Testing Center of Chongqing University and Elio Vescovo and Anil Rajapitamahuni of NSLS II for their assistance with measurements.

[1] C. Song, J. Park, J. Koo, K.-B. Lee, J. Y. Rhee, S. L. Bud'ko, P. C. Canfield, B. N. Harmon, and A. I. Goldman, Charge-density-wave orderings in $LaAgSb_2$: An x-ray scattering study, Phys. Rev. B **68**, 035113 (2003).

[2] K. Akiba, N. Umeshita, and T. C. Kobayashi, Observation of superconductivity and its enhancement at the charge density wave critical point in $LaAgSb_2$, Phys. Rev. B **106**, L161113 (2022).

[3] X. Shi, P. Richard, K. Wang, M. Liu, C. E. Matt, N. Xu, R. S. Dhaka, Z. Ristic, T. Qian, Y.-F. Yang, C. Petrovic, M. Shi, and H. Ding, Observation of Dirac-like band dispersion in $LaAgSb_2$, Phys. Rev. B **93**, 081105(R) (2016).

[4] S.-H. Baek, S. L. Bud'ko, P. C. Canfield, F. Borsa, and B. J. Suh, NMR evidence for a Peierls transition in the layered square-net compound $LaAgSb_2$, Phys. Rev. B **106**, 195153 (2022).

[5] A. Bosak, S.-M. Souliou, C. Faugeras, R. Heid, M. R. Molas, R.-Y. Chen, N.-L. Wang, M. Potemski, and M. Le Tacon, Evidence for nesting-driven charge density wave instabilities in the quasi-two-dimensional material $LaAgSb_2$, Phys. Rev. Res. **3**, 033020 (2021).

[6] K. Wang and C. Petrovic, Multiband effects and possible Dirac states in $LaAgSb_2$, Phys. Rev. B **86**, 155213 (2012).

[7] K. Akiba, N. Umeshita, and T. C. Kobayashi, Magnetotransport studies of the Sb square-net compound $LaAgSb_2$ under high pressure and rotating magnetic fields, Phys. Rev. B **105**, 035108 (2022).

[8] S. Klemenz, S. Lei, and L. M. Schoop, Topological semimetals in square-net materials, Annu. Rev. Mater. Res. **49**, 185 (2019).

[9] Y. Xia, L. Wang, Y. Zhu, L. Zhang, Y. Liu, X. Wu, L. Zhang, T. Yang, K. Yang, M. He, Y. Chai, H. Fu, X. Zhou, and A. Wang, Coupling between the spatially separated magnetism and the topological band revealed by magnetotransport measurements on $EuMn_{1-x}Zn_xSb_2$ ($0 \leqslant x \leqslant 1$), Phys. Rev. B **108**, 165115 (2023).

[10] Y. Muro, N. Takeda, and M. Ishikawa, Magnetic and transport properties of dense Kondo systems, $CeTSb_2$ (T = Ni, Cu, Pd and Ag), J. Alloys Compd. **257**, 23 (1997).

[11] J. R. Chamorro, A. Topp, Y. Fang, M. J. Winiarski, C. R. Ast, M. Krivenkov, A. Varykhalov, B. J. Ramshaw, L. M. Schoop, and T. M. McQueen, Dirac fermions and possible weak antilocalization in $LaCuSb_2$, APL Mater. **7**, 121108 (2019).

[12] K. Akiba and T. C. Kobayashi, Phonon-mediated superconductivity in the Sb square-net compound $LaCuSb_2$, Phys. Rev. B **107**, 245117 (2023).

[13] F. Du, H. Su, S. S. Luo, B. Shen, Z. Y. Nie, L. C. Yin, Y. Chen, R. Li, M. Smidman, and H. Q. Yuan, Interplay between charge density wave order and superconductivity in $LaAuSb_2$ under pressure, Phys. Rev. B **102**, 144510 (2020).

[14] C. N. Kuo, D. Shen, B. S. Li, N. N. Quyen, W. Y. Tzeng, C. W. Luo, L. M. Wang, Y. K. Kuo, and C. S. Lue, Characterization of the charge density wave transition and observation of the amplitude mode in $LaAuSb_2$, Phys. Rev. B **99**, 235121 (2019).

[15] L. Xiang, D. H. Ryan, W. E. Straszheim, P. C. Canfield, and S. L. Bud'ko, Tuning of charge density wave transitions in $LaAu_xSb_2$ by pressure and Au stoichiometry, Phys. Rev. B **102**, 125110 (2020).

[16] L. Xiang, D. H. Ryan, P. C. Canfield, and S. L. Bud'ko, Effects of physical and chemical pressure on charge density wave transitions in $LaAg_{1-x}Au_xSb_2$ single crystals, Crystals **12**, 1693 (2022).

[17] K. D. Myers, S. L. Bud'ko, V. P. Antropov, B. N. Harmon, P. C. Canfield, and A. H. Lacerda, de Haas–van Alphen and Shubnikov–de Haas oscillations in $RAgSb_2$ (R = Y, La-Nd, Sm), Phys. Rev. B **60**, 13371 (1999).

[18] G. Kresse and J. Furthmüller, Efficient iterative schemes for *ab initio* total-energy calculations using a plane-wave basis set, Phys. Rev. B **54**, 11169 (1996).

[19] G. Kresse and J. Furthmüller, Efficiency of *ab-initio* total energy calculations for metals and semiconductors using a plane-wave basis set, Comput. Mater. Sci. **6**, 15 (1996).

[20] J. P. Perdew, K. Burke, and M. Ernzerhof, Generalized gradient approximation made simple, Phys. Rev. Lett. **77**, 3865 (1996).

[21] P. E. Blöchl, Projector augmented-wave method, Phys. Rev. B **50**, 17953 (1994).

[22] A. M. Ganose, A. Searle, A. Jain, and S. M. Griffin, IFermi: A python library for Fermi surface generation and analysis, J. open source softw. **6**, 3089 (2021).

[23] O. Prakash, A. Thamizhavel, and S. Ramakrishnan, Ferromagnetic ordering of minority Ce^{3+} spins in a quasi-skutterudite $Ce_3Os_4Ge_{13}$ single crystal, Phys. Rev. B **93**, 064427 (2016).

[24] X. Teng, L. Chen, F. Ye, E. Rosenberg, Z. Liu, J.-X. Yin, Y.-X. Jiang, J. S. Oh, M. Z. Hasan, K. J. Neubauer, B. Gao, Y. Xie, M. Hashimoto, D. Lu, C. Jozwiak, A. Bostwick, E. Rotenberg, R. J. Birgeneau, J.-H. Chu, M. Yi, and P. Dai, Discovery of charge density wave in a kagome lattice antiferromagnet, Nature (London) **609**, 490 (2022).

[25] C. S. Lue, Y. F. Tao, K. M. Sivakumar, and Y. K. Kuo, Weak charge-density-wave transition in $LaAgSb_2$ investigated by transport, thermal, and NMR studies, J. Phys.: Condens. Matter **19**, 406230 (2007).

[26] A. Pippard, *Magnetoresistance in Metals*, Cambridge Studies in Low Temperature Physics (Cambridge University Press, Cambridge, 1989).

[27] I. Pletikosić, M. N. Ali, A. V. Fedorov, R. J. Cava, and T. Valla, Electronic structure basis for the extraordinary magnetoresistance in WTe_2, Phys. Rev. Lett. **113**, 216601 (2014).

[28] D. Stroud and F. P. Pan, Magnetoresistance and Hall coefficient of inhomogeneous metals, Phys. Rev. B **20**, 455 (1979).

[29] J. Hu and T. F. Rosenbaum, Classical and quantum routes to linear magnetoresistance, Nat. Mater. **7**, 697 (2008).

[30] M. Kohler, Zur magnetischen Widerstandsänderung reiner Metalle, Annalen der Physik **424**, 211 (1938).

[31] R. H. McKenzie, J. S. Qualls, S. Y. Han, and J. S. Brooks, Violation of Kohler's rule by the magnetoresistance of a quasi-two-dimensional organic metal, Phys. Rev. B **57**, 11854 (1998).

[32] P. Knowles, B. Yang, T. Muramatsu, O. Moulding, J. Buhot, C. J. Sayers, E. Da Como, and S. Friedemann, Fermi surface reconstruction and electron dynamics at the charge-density-wave transition in $TiSe_2$, Phys. Rev. Lett. **124**, 167602 (2020).

[33] K. Noto, S. Morohashi, K. Arikawa, and Y. Muto, Temperature and magnetic field dependence of the electrical resistance in pure and Fe-doped 2H-$NbSe_2$, Physica B+C **99**, 204 (1980).

[34] R. A. Smith, *Semiconductors*, 2nd ed. (Cambridge University Press, New York, 1978).

[35] D. Shoenberg, *Magnetic Oscillations in Metals*, Cambridge Monographs on Physics (Cambridge University Press, Cambridge, 1984).

[36] J. B. He, Y. Fu, L. X. Zhao, H. Liang, D. Chen, Y. M. Leng, X. M. Wang, J. Li, S. Zhang, M. Q. Xue, C. H. Li, P. Zhang, Z. A. Ren, and G. F. Chen, Quasi-two-dimensional massless Dirac fermions in $CaMnSb_2$, Phys. Rev. B **95**, 045128 (2017).

[37] J. Y. Liu, J. Hu, Q. Zhang, D. Graf, H. B. Cao, S. M. A. Radmanesh, D. J. Adams, Y. L. Zhu, G. Cheng, X. Liu, W. A. Phelan, J. Wei, M. Jaime, F. Balakirev, D. A. Tennant, J. F. DiTusa, I. Chiorescu, L. Spinu, and Z. Q. Mao, A magnetic topological semimetal $Sr_{1-y}Mn_{1-z}Sb_2$ (y, z < 0.1), Nature Mater. **16**, 905 (2017).

[38] S. Huang, J. Kim, W. A. Shelton, E. W. Plummer, and R. Jin, Nontrivial Berry phase in magnetic $BaMnSb_2$ semimetal, Proc. Natl. Acad. Sci. USA **114**, 6256 (2017).

[39] Y.-Y. Wang, S. Xu, L.-L. Sun, and T.-L. Xia, Quantum oscillations and coherent interlayer transport in a new topological Dirac semimetal candidate $YbMnSb_2$, Phys. Rev. Mater. **2**, 021201(R) (2018).

[40] J. Hu, S.-Y. Xu, N. Ni, and Z. Mao, Transport of topological semimetals, Annu. Rev. Mater. Res. **49**, 207 (2019).

[41] See Supplemental Material at http://link.aps.org/supplemental/10.1103/PhysRevB.108.245156. for magnetization, DOS, and more details of calculated Fermi surface.

[42] M. Rosmus, N. Olszowska, Z. Bukowski, P. Starowicz, P. Piekarz, and A. Ptok, Electronic band structure and surface states in dirac semimetal $LaAgSb_2$, Materials **15**, 7168 (2022).

[43] I. Hase and T. Yanagisawa, Electronic band calculation of $LaTSb_2$ (T = Cu,Ag,Au), Phys. Procedia. **58**, 42 (2014).

[44] T. Valla, A. V. Fedorov, P. D. Johnson, P.-A. Glans, C. McGuinness, K. E. Smith, E. Y. Andrei, and H. Berger, Quasiparticle spectra, charge-density waves, superconductivity, and electron-phonon coupling in 2H-$NbSe_2$, Phys. Rev. Lett. **92**, 086401 (2004).

[45] T. Valla, A. V. Fedorov, J. Lee, J. C. Davis, and G. D. Gu, The ground state of the pseudogap in cuprate superconductors, Science **314**, 1914 (2006).

[46] Y. Feng, Z. Wang, C. Chen, Y. Shi, Z. Xie, H. Yi, A. Liang, S. He, J. He, Y. Peng, X. Liu, Y. Liu, L. Zhao, G. Liu, X. Dong, J. Zhang, C. Chen, Z. Xu, X. Dai, Z. Fang, and X. J. Zhou, Strong anisotropy of Dirac cones in $SrMnBi_2$ and $CaMnBi_2$ revealed by angle-resolved photoemission spectroscopy, Sci. Rep. **4**, 5385 (2015).

[47] S. Borisenko, D. Evtushinsky, Q. Gibson, A. Yaresko, K. Koepernik, T. Kim, M. Ali, J. van den Brink, M. Hoesch, A. Fedorov, E. Haubold, Y. Kushnirenko, I. Soldatov, R. Schäfer, and R. J. Cava, Time-reversal symmetry breaking type-II Weyl state in $YbMnBi_2$, Nat. Commun. **10**, 3424 (2019).

[48] K. Zhao, E. Golias, Q. H. Zhang, M. Krivenkov, A. Jesche, L. Gu, O. Rader, I. I. Mazin, and P. Gegenwart, Quantum oscillations and Dirac dispersion in the $BaZnBi_2$ semimetal guaranteed by local Zn vacancy order, Phys. Rev. B **97**, 115166 (2018).

[49] S. Thirupathaiah, D. Efremov, Y. Kushnirenko, E. Haubold, T. K. Kim, B. R. Pienning, I. Morozov, S. Aswartham, B. Büchner, and S. V. Borisenko, Absence of Dirac fermions in layered $BaZnBi_2$, Phys. Rev. Mater. **3**, 024202 (2019).

[50] L. M. Schoop, M. N. Ali, C. Straßer, A. Topp, A. Varykhalov, D. Marchenko, V. Duppel, S. S. P. Parkin, B. V. Lotsch, and C. R. Ast, Dirac cone protected by non-symmorphic symmetry and three-dimensional Dirac line node in ZrSiS, Nat. Commun. **7**, 11696 (2016).

[51] T. Liang, Q. Gibson, M. N. Ali, M. Liu, R. J. Cava, and N. P. Ong, Ultrahigh mobility and giant magnetoresistance in the Dirac semimetal Cd_3As_2, Nature Mater. **14**, 280 (2015).

[52] Z. K. Liu, J. Jiang, B. Zhou, Z. J. Wang, Y. Zhang, H. M. Weng, D. Prabhakaran, S.-K. Mo, H. Peng, P. Dudin, T. Kim, M. Hoesch, Z. Fang, X. Dai, Z. X. Shen, D. L. Feng, Z. Hussain, and Y. L. Chen, A stable three-dimensional topological Dirac semimetal Cd_3As_2, Nature Mater. **13**, 677 (2014).

[53] M. Neupane, S.-Y. Xu, R. Sankar, N. Alidoust, G. Bian, C. Liu, I. Belopolski, T.-R. Chang, H.-T. Jeng, H. Lin, A. Bansil, F. Chou, and M. Z. Hasan, Observation of a three-dimensional topological Dirac semimetal phase in high-mobility Cd_3As_2, Nat. Commun. **5**, 3786 (2014).

[54] B. R. Ortiz, S. M. L. Teicher, Y. Hu, J. L. Zuo, P. M. Sarte, E. C. Schueller, A. M. Milinda Abeykoon, M. J. Krogstad, S. Rosenkranz, R. Osborn, R. Seshadri, L. Balents, J. He, and S. D. Wilson, CsV_3Sb_5: A Z_2 topological kagome metal with a superconducting ground state, Phys. Rev. Lett. **125**, 247002 (2020).

[55] L. Nie, K. Sun, W. Ma, D. Song, L. Zheng, Z. Liang, P. Wu, F. Yu, J. Li, M. Shan, D. Zhao, S. Li, B. Kang, Z. Wu, Y. Zhou, K. Liu, Z. Xiang, J. Ying, Z. Wang, T. Wu, and X. Chen, Charge-density-wave-driven electronic nematicity in a kagome superconductor, Nature (London) **604**, 59 (2022).

[56] H. W. S. Arachchige, W. R. Meier, M. Marshall, T. Matsuoka, R. Xue, M. A. McGuire, R. P. Hermann, H. Cao, and D. Mandrus, Charge density wave in kagome lattice intermetallic ScV_6Sn_6, Phys. Rev. Lett. **129**, 216402 (2022).

[57] H. Tan, Y. Liu, Z. Wang, and B. Yan, Charge density waves and electronic properties of superconducting kagome metals, Phys. Rev. Lett. **127**, 046401 (2021).